Molecular interactions between gelatin-derived carbon quantum dots and Apo-myoglobin: Implications for carbon nanomaterial frameworks

Shima Masoudi Asil[a], **Mahesh Narayan**[b,*]

[a]The Environmental Science & Engineering Program, The University of Texas at El Paso, El Paso, TX 79968, USA

[b]The Department of Chemistry & Biochemistry, The University of Texas at El Paso, El Paso, TX 79968, USA

Abstract

Carbon nanomaterials (CNMs), including carbon quantum dots (CQDs), have found widespread use in biomedical research due to their low toxicity, chemical tunability, and tailored applications. Yet, there exists a gap in our understanding of the molecular interactions between biomacromolecules and these novel carbon-centered platforms. Using gelatin-derived CQDs as a model CNM, we have examined the impact of this exemplar nanomaterial on apo-myoglobin (apo-Mb), an oxygen-storage protein. Intrinsic fluorescence measurements revealed that the CQDs induced conformational changes in the tertiary structure of native, partially unfolded, and unfolded states of apo-Mb. Titration with CQDs also resulted in significant changes in the secondary structural elements in both native (holo) and apo-Mb, as evidenced by the circular dichroism (CD) analyses. These changes suggested a transition from isolated helices to coiled-coils during the loss of the helical structure of the apo-protein. Infra-red spectroscopic data further underscored the interactions between the CQDs and the amide backbone of apo-myoglobin. Importantly, the CQDs-driven structural perturbations resulted in compromised heme binding to apo-myoglobin and, therefore, potentially can attenuate oxygen storage and diffusion. However, a cytotoxicity assay demonstrated the continued viability of neuroblastoma cells exposed to these carbon nanomaterials. These results, for the first time, provide a molecular roadmap of the interplay between carbon-based nanomaterial frameworks and biomacromolecules.

Keywords

Carbon quantum dots; Protein structure; Folding/unfolding; Nanotechnology; Apo-myoglobin

1. Introduction

Nanoparticles (NPs), including carbon nanomaterials (CNMs) have found widespread use in biological applications [1-3]. CNMs including fullerenes, carbon dots (CDs), carbon quantum dots (CQDs), graphene quantum dots (GQDs), and carbon nano onions (CNOs), have been used for diverse purposes, including theragnostics for biological and environmental detection, sensing, and imaging [4-7]. They have also demonstrated potential as antivirals in tissue engineering and cancer therapy, and even as nanofertilizers [8-13].

CQDs are of particular interest in the aforementioned areas of biomedicine given their ease of synthesis, chemical tunability, ability to scavenge reactive oxygen species, imaging ability, and high biocompatibility [14,15]. Recent work has demonstrated that CQDs dissolve mature amyloid fibrils and also prevent the soluble-to-toxic transformation of amyloid-fibril-forming proteins [16-18]. Data from our laboratory have revealed that they are able to intervene across multiple targets in the trajectory of Parkinson's [19-21]. Functionalized GQDs intervened in the soluble-to-toxic transformation of the Parkinsonian amyloid α-synuclein [22,23]. Appropriately functionalized CQDs, GQDs, and other CNMs are able to cross the blood-brain barrier (BBB), making them particularly attractive in prophylaxis and therapy [24-29].

The impact of different types of NPs, including CNMs, on human health has not been sufficiently underscored. Considering the rapid growth of nanobiotechnology and the application of CNMs across the biome [30,31], it is critical to examine interactions between CQDs and biomolecules such as proteins, DNA, lipids, and carbohydrates. Proteins, vital macromolecules in living systems, can bind to ligands, even at the nano-scale level, giving rise to complex interactions and triggering structural changes in the protein. When NPs enter biological systems, they interact with proteins on their surfaces, leading to the formation of NP-biomolecule complexes that govern their biological effects [32,33] (Fig. 1). Proteins adhered to NPs can undergo conformational changes, impacting their structure and function [34,35]. Various NPs have shown different interactions with biomolecules. As an illustration, gold nanoparticles have a significant affinity for essential blood proteins such as albumin, fibrinogen, α-globulin, histone, and insulin, resulting in conformational changes in these proteins [36-38]. A recent study examining the interaction between vinegar carbon dots (VCDs) with human plasma protein (HHB) using FTIR, atomic force microscopy, and circular dichroism analysis showed alterations in HHB upon its binding with VCDs [39]. Understanding these changes is of utmost importance as it provides valuable insights into the proteins' role in different fields, including biochemistry, medicinal chemistry, and nanobiotechnology. However, there continues to remain a gap in our comprehensive understanding of these implications and the associated risks [40].

Here, we have examined the impact of CQDs on a model protein in an attempt to advance a molecular level understanding of the interactions between CQDs and biomolecules. There are a number of reasons that motivate this study: 1) As aforementioned, in addition to their biological targets, CQDs are likely to interact with off-target molecules. Therefore, the characterization of these interactions provides insight into the role of CQDs in modulating

cellular homeostasis, attenuating pathways that "off-target" molecules may be involved in, and influencing the biological activities of molecules that CQDs come in contact with. 2) It can provide information about biological safety regarding the use of CQDs. 3) Understanding the impact of CQDs on protein structure facilitates understanding how CQDs intervene in the soluble-to-toxic conversion of amyloid proteins, information critical to transitioning CQDs into pre-clinical and clinical trials. 4) Lastly, understanding the CQDs' interaction with biomolecules facilitates the design of 2nd generation CQDs that are not only more biologically effective but also demonstrate enhanced target specificity.

Gelatin-derived CQDs were chosen as a representative CQD along with apo-myoglobin, a small predominantly α-helical globular protein, as the model protein for studying the interaction between CQDs and biomolecules. Gelatin, being a widely available, biocompatible, and cost-effective biomaterial, presented an attractive starting point for CQD synthesis which aligned with our study's focus on exploring environmentally friendly and sustainable materials for potential biomedical applications. Gelatin-derived CQDs possess carbonyl, carboxylic, and hydroxyl surface-functional groups centered around a carbon core. They attenuate pesticide-associated mortality in *C. elegans* while protecting the nematode dopaminergic neurons from pesticide-induced ablation [19-21]. It is therefore germane to this study given its prior use.

Myoglobin is a 153 amino acid heme-containing protein associated with the storage of oxygen. The protein exhibits >70 % helicity with negligible beta-sheet content, making it a prototype model for examining the role of CQDs on the helical structures of proteins [41-45]. However, the fluorescence of tryptophan in myoglobin is quenched due to the proximity of the heme group. This is because the excited-state energy of tryptophan can be transferred non-radiatively to the heme group, leading to a decrease in the fluorescence intensity of tryptophan. Removing the heme group can eliminate this energy transfer process and increase the fluorescence intensity of tryptophan. Apo-myoglobin, or heme-free myoglobin, possesses ~55 % helical structure and <10 % beta-sheet content [46]. Therefore, to evaluate CQDs' impacts on conformational changes of protein through the intrinsic fluorescence of tryptophan, we have selected apo-myoglobin. The binding of heme to apo-myoglobin to form myoglobin provides the protein with oxygen storage capacity (Fig. 2). Therefore, the selection of apo-myoglobin facilitates the underscoring of CQDs' impact on protein function. Furthermore, by examining the CQDs' impact on apo-myoglobin secondary structure, we are able to study the system in a relatively isolated condition without interfering with confounding variables, such as the presence of beta-strands and sheets.

The study aimed to investigate the impact of CQDs on diverse protein structures, encompassing the native state as well as partially folded or unfolded states. Our hypothesis involved assessing the effect of CQDs on proteins in semi-folded states, aiming to understand these materials' capability in either restoring the native protein structure or worsening the condition by inducing further protein unfolding. To explore this hypothesis, we utilized varying concentrations of urea to induce different degrees of protein unfolding. This allowed us to examine whether CQDs could potentially mitigate or exacerbate these unfolding processes.

Lastly, to evaluate the safety of these carbon nanomaterials at the cellular level, we investigated the gelatin-derived CQDs-induced toxicity against neuroblastoma cell lines (SH-SY5Y) using a cytotoxicity assay. Neuroblastoma cell lines, which resemble neurons, are extensively utilized in conducting cytotoxicity assays induced by nanoparticles [47,48].

2. Materials and methods

2.1. Chemicals and materials

All chemicals were obtained commercially including Tris-HCl (Millipore-Sigma, MO, USA), myoglobin (from equine skeletal muscle- type A), Urea (Fisher Scientific, NJ, USA), 2-butanone (Fisher Scientific, Waltham, MA, USA) Gelatin (from porcine skin) (Sigma-Aldrich, MO, USA), Cell culture media DMEM/F-12 (Dulbecco's Modified Eagle Medium/Nutrient Mixture F-12) (Millipore-Sigma, USA), Hoechst 33342 fluorescent stain (Invitrogen, Carlsbad, CA, USA), Propidium iodide (PI) (Invitrogen, Eugene, OR, USA), Fetal Bovine Serum (FBS) (Atlanta Biologicals, Atlanta, GA, USA). Dialysis bags (3 kDa) (Fisher Scientific, Waltham, MA, USA) and microfilters (0.22 μM) (Fisher Scientific, Waltham, MA, USA). All the dilutions including gelatin-CQDs and apo-myoglobin, were made with high purity de-ionized water (18 MΩ cm^{-1} resistivity) obtained from a Milli-Q water purification system (Millipore, Bedford, MA, USA).

2.2. Synthesis of carbon quantum dots

2.2.1. Gelatin CQDs—To synthesize the gelatin CQDs, the procedures previously described were followed [20]. Briefly, 0.8 g of gelatin (molecular weight: 100 kDa) was dissolved in 40 mL of Milli-Q water and placed on a hot plate at 40 °C with stirring until the gelatin powder completely dissolved and formed a clear, homogeneous solution. This process took approximately 10 min. Subsequently, the mixture was transferred into a hydrothermal bomb with a Teflon liner of 50 mL capacity and placed in the oven at 200 °C for 3 h. The bomb was allowed to cool to room temperature. To remove large nanoparticles and aggregates, the final yellowish solution was centrifuged at 16,000 rpm for 30 min, and the light brown aqueous solution was filtered using 0.2 μm microfilters. The final product was lyophilized prior to storage.

2.3. Characterization of CQDs

Absorption spectra were recorded using a Genesys 10s UV–Vis spectrophotometer (Thermo Scientific). Fluorescence spectra were recorded using a DM45 Olis spectrofluorometer equipped with a water bath set at 24 °C. DLS measurements were performed with a Malvern Zetasizer Nano ZS90 at room temperature. IR data were collected at room temperature using a BRUKER spectrometer (TENSOR 27, USA). Transmission electron microscopy (TEM) imaging of CQDs was performed with a high-resolution TEM (HR-TEM, JEOL 2010F) at UNAM University.

2.4. Preparation of apo-myoglobin from myoglobin

The heme group was extracted from horse skeletal muscle myoglobin (Mb) by the 2-butanone extraction method as previously described [49]. Briefly, the pH of myoglobin solution (100 mg Mb in 40 mL Milli-Q water) was first adjusted to 2.5 in an ice-water

bath using chilled 0.1 M HCl (aq). In a separation funnel, the myoglobin solution and an equal volume of 2-butanone were gently shaken and allowed to stand for 10 min at 4 ° C. Then, the colorless aqueous phase was separated and dialyzed using dialysis bags (molecular weight cut-off 1000 Da) for 24 h at 4 °C against 5 L of Milli-Q water and a further 24 h against PBS buffer (pH 7.3). Next, the solution was filtered using a 0.22 μm microfilter and the final product was lyophilized for long-time storage. The concentration of prepared apo-Mb was spectrophotometrically determined using its extinction coefficient of 15,700 M^{-1} cm^{-1} at 280 nm [50].

2.5. Fluorescence measurements

For protein folding-unfolding experiments, fluorescence spectra between 300 and 400 nm at bandwidths of 0.5 nm with excitation at 280 nm were recorded at 25 °C on a DM45 Olis spectrofluorometer in the scan mode. Emission spectra were recorded by dissolving the protein in a 100 mM Tris-HCl buffer (pH 7.0). For urea treatment, proteins were diluted in various concentrations of urea. Urea solutions ranging from 1 to 5 M were prepared using urea dissolved in a 100 mM Tris-HCl buffer. Apo-myoglobin (1 mg. mL^{-1}) was incubated with the different concentrations of gelatin CQDs (0, 0.1, 0.15, 0.2, 0.35, 0.5, and 1 mg. mL^{-1}) for 30 min prior to reading the emission spectra. The protein concentration remained constant at 1 mg. mL^{-1} for all treatments. The tryptophan fluorescence intensities of the CQDs-protein mixtures were corrected for the inner filter effect using the following formula [51]:

$$F_1 = F_0 \times e^{\wedge((abs.280 + abs.\,max \text{ emission})\,/\,2)}$$

where F_1 is corrected fluorescence, F_0 is maximum measured fluorescence, *280* is absorption at 280 nm and *abs. max emission* is the absorbance in the maximum emitted wavelength.

Differences in maximum fluorescence intensity between the free protein and CQDs-protein (excitation at 280 nm) were analyzed to observe any shift or change of intensity in the maximum fluorescence wavelength.

2.6. Circular dichroism measurement

For analyzing the secondary structure of apo-myoglobin (1 mg. mL^{-1}) as a function of CQDs (0, 0.1, 0.15, 0.2, 0.35, 0.5, and 1 mg. mL^{-1}), circular dichroism (CD) spectra were recorded at 25 °C using a bandwidth of 1 nm, a step interval of 1 nm, and a scan rate of 50 nm. min^{-1}, and a slit width of 0.02 mm (JASCO J-1500, USA). A quartz cell with a 0.1 mm path length was used for far-UV (range of 190-260 nm) measurements. Here, different concentrations of gelatin-derived CQDs, ranging from 0 to 1 mg. mL^{-1} were mixed with 1 mg. mL^{-1} (6 μM) of protein in 5 mM Tris-HCl buffer for native proteins or in 1.5 M urea for semi-folded proteins. The CQDs were added to the protein solution and incubated for 30 ± 5 min before recording spectra. Three scans of triplicate samples were measured and averaged. Control buffer scans were run in triplicate, averaged, and then subtracted from the sample spectra.

2.7. Fourier transform infrared spectroscopy (FTIR)

Apo-myoglobin (6 μm) was prepared in 5 mM Tris-HCl. FTIR spectra were recorded using a BRUKER Tensor 27 FTIR spectrometer in absorbance mode. The protein was then titrated with CQDs, and measurements were repeated (30 min after the addition of CQDs). The spectra were measured for each sample with the buffer solution as the blank (background) spectrum. The spectra of protein alone or protein-CQDs mixtures were separately corrected by subtracting them from the background spectrum. The data obtained were the absorbance spectra for the samples in the 4000–500 cm^{-1} spectral wave numbers. The spectra of the amide I region (1700–1600 cm^{-1}) were analyzed using Gaussian deconvolution of FTIR spectrum in OriginPro software.

2.8. Heme binding assay

The kinetics of apo-Mb-Heme interaction was measured using the absorbance changes at 409 nm upon heme binding to apo-myoglobin as described elsewhere [52,53]. Apo-Mb-Heme binding experiments were performed using a UV–visible spectrophotometer (Thermo Scientific) by following the formation of myoglobin (from apo-myoglobin) at 409 nm. Heme was first dissolved in a minimal volume of 0.1 M NaOH to solubilize it and then diluted with Milli-Q water to about 1 mM. The apo-Mb-Heme complexes (1:5) were prepared by mixing apo-myoglobin (final concentration of 10 μM), and hemin solutions (final concentration of 50 μM) in phosphate buffer (100 mM, pH 7.6) supplemented with 2.5 % glycerol. The apo-myoglobin solution was placed in the sample cell of the spectrophotometer, and the apo-Mb-Heme complex (myoglobin) was generated upon the addition of the heme solution. The apo-Mb-Heme-CQDs binding reaction was conducted under the same conditions, except that the apo-myoglobin solution was pre-treated with 1 mg. mL^{-1} CQDs at room temperature for 5 min. Data were collected for 60 s and 2.5 h for the fast and slow binding phases, respectively. Data were normalized by subtracting the baseline at 409 nm (autozero prior to measurement), and the k constants were calculated by fitting the data to the pseudo-first-order equation to model the kinetics of heme adsorption onto the apo-myoglobin.

2.9. Cell culture

Human neuroblastoma cells (SH-SY5Y (ATCC, Manassas, VA)) were grown in a pre-prepared cell-culture medium (DMEM/F-12, 398225 SIGMA) and supplemented with 10 % fetal bovine serum and 1 % penicillin [16,19-21]. Cells were maintained by incubation at 37 °C with 5 % carbon dioxide in a T75 flask. Cells were seeded into a 96-well plate and incubated until confluency was achieved. Once confluent, the cells were treated with the synthesized CQDs (100 μg. mL^{-1} to 10 mg. mL^{-1}) for 24 h. Alongside CQDs treatment, untreated (negative control), vehicle (H$_2$O), and hydrogen peroxide (H$_2$O$_2$) (positive control) groups were incubated in the same plate for 24 h before microscopic analysis.

2.10. Measuring cytotoxicity

Cytotoxicity of gelatin CQDs was determined by seeding SHSY-5Y (10,000 cells/well) into 96-well plates as previously described [16,19-21]. After the cells reached 80 % to 90 % confluency, CQDs were introduced to determine their possible cytotoxic effect. Treatments

on the plate were divided as the control for nonspecific effects, H_2O as the vehicle, and hydrogen peroxide as an insult. To read the plate, a mixture of dyes, propidium iodide (red-fluorescent, permeant only to dead cells, and commonly used to detect dead cells in a population [54]), and Hoechst (33342) (blue fluorescent, cell-permeable, and used to stain live cells in a population [55]) effective at a final concentration of 1 μg. mL^{-1} were added to each well one hour before obtaining readings. Image acquisition was acquired in a live-cell mode using a multi-well plate reader, the BD Pathway 855 confocal automated microscope system (GE Healthcare) equipped with 10× objective, and a BD Pathway analyzer 2000 acquisition v4.0 software (GE Healthcare). Four contiguous fields with a montage of (3 × 3) were acquired per well and per fluorescence channel. Image capture and data analysis were translated into a BD Pathway analyzer workstation v3.7.2 software (GE Healthcare) which was used for segmentation of the images to provide the region of interest and obtain the cytotoxicity percentages of cell death per each well.

2.11. Statistical analysis

The results of all assays were expressed as mean ± S.D. (Standard Deviation of Mean) and processed by commercially available software IBM SPSS Statistics 22. One-way ANOVA followed by post-hoc analysis was performed for the cytotoxicity test. Comparisons were made at a significance level of 1 % ($P < 0.01$).

3.   Results and discussion

The UV–Vis spectrum of myoglobin displays a characteristic Soret absorption maximum at 409 nm that corresponds to bound heme (Fig. S1, red graph) [50]. By contrast, the removal of the heme results in the complete diminution (elimination) of the Soret band (Fig. S1, green graph) with the concomitant formation of apo-myoglobin. Addition of the heme back to the solution of apo-myoglobin results in the slow recovery of absorbance at 409 nm. The slow increase in absorbance at 409 nm, indicating the recovery upon heme addition to apo-myoglobin, is demonstrated in Fig. 11A and B, including graphs for the control (apo-heme recovery without CQDs). These figures illustrate the rate of heme binding to apo-myoglobin. This rise in absorbance correlates with the incorporation of heme molecules, subsequently reflected in the UV–Vis spectra resembling the red graph depicted in Fig. S1, representing the full myoglobin complex (heme bound to apo-myoglobin).

3.1. Gelatin CQDs characterization

CQDs were synthesized using gelatin as the carbon source [20]. There are several studies which indicate that the size, surface chemistry, and charge of the CQDs can affect their properties [56-59].

The CQDs displayed a relatively homogeneous size distribution as evidenced by HR-TEM analysis (Fig. 3A). A lattice spacing of 0.33 nm was recorded (Inset to Fig. 3A). The XRD analysis depicted a broad peak around 26 degrees (Fig. 3B), indicative of an amorphous or less crystalline structure, in alignment with previous studies highlighting the disordered nature of these nanomaterials [60]. However, the HR-TEM imaging revealed some areas with faint lattice fringes (Inset to Fig. 3A), suggesting the presence of some ordered regions

within the CQDs. These lattice spacings, although intermittent and less prevalent, appeared as faint fringes in localized areas. As is typical of CQDs, the size range of the nanomaterials resided between 1.5 and 5 nm. The analysis of the size distribution revealed a Gaussian profile with ~30 % of the particles centered around 3.5 nm and >80 % of the CQDs of size between 2 and 4 nm (Fig. 3C), in agreement with HR-TEM data and previously reported values for CQDs from various carbon materials [61,62]. DLS measurements (Fig . 3D) revealed an average size of ~4.8 nm with a dispersion between 2.8 and 7.5 nm. The obtained zeta potential results revealed that the CQDs have potential of −35mV (Fig. 3E), which prevent the particles from agglomeration and suggest their relatively good stability. The negative zeta potential can be assigned to carboxylic acid functional groups at the surface of the CQDs (Fig. S2 in ESM).

The absorption spectrum of gelatin CQDs is shown in Fig. 4A. The CQDs exhibit a broad peak between 250 and 290 nm which can typically be ascribed to the absorption of an aromatic p system or the ρ-π^* transition of the carbonyl group [16]. Furthermore, the lingering absorption of the nanomaterials up to 450 nm suggests the presence of an extensive sp^2 hybridized network of carbon atoms. The inset to Fig. 4A shows that gelatin-derived CQDs are colorless and clear when viewed by the naked eye under ambient light conditions.

The fluorescence emission spectrum displays a maximum peak at 430 nm when excited at 345 nm (Fig. 4B). An aqueous suspension of CQDs exhibits an intense blue emission under UV light, which could be easily visualized with the naked eye (Inset to Fig. 4B).

The emission spectra also demonstrate an excitation-dependent shift in emission maximum, as illustrated in Fig. 4C. The most intense emission peak occurs at 430 nm (Exc. 340 nm) and reduces in intensity as the maximum emission shifts to 535 nm as a function of an increase in the excitation wavelength from 300 nm to 480 nm. The main fluorescence mechanism observed in most CQDs is attributed to the surface-defect states induced by diverse surface-functional groups. The presence of multiple functional group combinations gives rise to intricate radiative relaxation processes, resulting in multicolor emissions and excitation-dependent emission characteristics [63]. Defects in carbon dots, encompassing surface defects and heteroatom doping, profoundly influence their fluorescence properties by acting as capture canters for excitons. These defects impact the energy gap and contribute to surface-state-related fluorescence [64,65]. The data indicate the presence of defect centers in the CQDs and/or the presence of multiple fluorophores, as is typically observed in such nanomaterials [16,19-21,66]. A contour plot of the fluorescence emission intensity was measured as a function of the excitation wavelength ranging from 280 to 440 nm, and its intensity was indicated as a "*Z*-scale" (Fig. 4D). The data confirms that emission occurs at wavelengths higher than 400 nm even when excited at 300 nm, suggesting highly conjugated systems comprising sp^2 hybridized frameworks in the gelatin CQDs.

An examination of the IR spectrum of the CQDs is in good agreement with previously reported results (Fig. S2 in ESM) [67-70]. The broad peak of O—H at 3400–3500 cm^{-1}, the stretching vibration bond of C=0 at 1700 cm^{-1}, and the stretching vibration bond of C—O at 1100 cm^{-1} suggest the presence of carboxylic acid and other oxygen-containing functional groups, which are responsible for the solubility of CQDs. The absorption peak

at 3065 cm^{-1} corresponds to the N—H group, and the peak at 1450 cm^{-1} is assigned to the vibration and deformation bonds of N—H, suggesting the existence of amino-functional groups. Lastly, the absorption peaks at 2920, 1400, and 1320 cm^{-1} are associated with the stretching vibrations of C—H, C≡C, and C—C, reflecting alkyl and aryl groups, respectively.

3.2. Impact of gelatin CQDs on the tertiary structure of apo-myoglobin

Conformational changes in the tertiary structure of proteins induced by interactions with nanomaterials can be monitored and characterized using intrinsic protein fluorescence [71]. The absence of fluorescence emitted from CQDs upon excitation at 280 nm (Fig. 4D) further supports the notion that shifts in emission solely rely on the intrinsic fluorescence of the protein. Fig. 5 shows the steady-state fluorescence spectrum of apo-myoglobin and apo-myoglobin titrated with gelatin-derived CQDs. A CQDs-dose-dependent increase in emission intensity is observed in apo-myoglobin. Furthermore, a gradual red-shift is induced by the nanomaterials. Over the course of the titration, the λ_{max} shifted from 334 nm (0.15 mg. mL^{-1} CQDs) to 336 nm (1 mg. mL^{-1} CQDs).

Interaction of proteins with nanoparticles has shown to result in the perturbation of their native conformation and subsequent dysfunction, particularly upon binding to the nanoparticles' hydrophobic regions [72]. The data reflect a CQDs-dose-dependent conformational change in the tertiary structure of apo-myoglobin. The red-shift observed during the titration suggests that CQDs introduction causes a partial unfolding of the protein. The CQDs-dependent increase in emission intensity may be attributed to the fact that in the absence of CQDs, the fluorescence of tryptophan (Trp) in apo-myoglobin is quenched, this is most likely because the Trp residue is deeply buried and shielded within the hydrophobic core of the protein, protecting it from the surrounding solvent. [73,74]. The CQDs-driven unfolding of the protein may lead to the exposure of Trp to the surrounding solvent and increasing Trp quantum yield along with the aforementioned red-shift.

The results are recapitulated in Fig. S3A (in ESM), where a gradual red-shift in emission maximum is observed as a function of CQDs dose. The significance of red shift in the maximum wavelength (λ_{max}) can be correlated with the degree of denaturation or unfolding within the protein structure. The more significant shift up to 0.2 mg mL^{-1} CQDs can be due to higher degree of disruption in native structure of protein which enhance the interaction frequency between the CQDs and the protein's binding sites. In higher concentration of CQDs (0.35 mg mL^{-1} and higher), there is still red shift in λmax which is less significant and can be stem from less stable proteins available in the environment to interact with CQDs.

Next, we examined the role of gelatin-derived CQDs on increasingly unfolded states of apo-myoglobin. Apo-myoglobin unfolding was induced by incubation with increasing urea concentrations ranging from 1 M to 5 M.

In the presence of 1 M urea, titration with CQDs (0.1–1 mg. mL^{-1}) resulted in a slight red-shift of 1 nm. The titration of apo-myoglobin in the presence of 2 M urea with CQDs mimicked the red shift in fluorescence emission maximum observed in the absence of urea.

A similar trend was observed when the titrations were performed under conditions with apo-myoglobin in the presence of 3 M and 5 M urea. By contrast, the results under 4 M conditions mimicked that seen in 1 M urea with only a 1 nm red-shift. Based on the results, it appears that the CQDs act similarly to a denaturant, such as urea, for the protein. Between 1 and 3 M urea, the protein's most native structure is denatured, as the apomyoglobin's midpoint concentration for unfolding is 2.6 M urea. Consequently, the unfolding induced by CQDs (which exacerbate urea's effect) in the range of 1–3 M urea is more pronounced than in 4 M urea, where approximately half of the protein has already undergone unfolding. The reason for a greater red-shift in CQDs + protein at 5 M urea (Fig. S3-F) compared to 4 M urea (Fig. S3-E) may be attributed to the proteins' increased instability, making them more susceptible to further disruption by CQDs. Consequently, the significant red-shift observed in 5 M urea with increasing CQDs concentrations signifies the instability of the protein structure at higher urea concentrations (5 M), potentially leading to complete unfolding of the protein.

An examination of the fluorescence intensity of apo-myoglobin as a function of CQDs on its increasingly unfolded states exhibited trends consistent with the steady-state spectra previously discussed (Fig. 6). In the absence of urea, the maximum fluorescence emission intensity increases uniformly as a function of CQDs dose (0.1–1 mg. mL^{-1}), which recapitulates the "dissociation" of Trp residues from their previously quenched environment. A similar trend is observed at higher stages of unfolding (1–3 M urea), where the addition of increasing amounts of gelatin-derived CQDs correlates with an increase in apo-myoglobin emission. In the presence of 4 M urea, an inversion in the CQDs-dependent fluorescence intensity profile is observed. The shallow decrease in intensity as a function of increasing CQDs concentration suggests that the Trp's are somewhat already solvent-exposed and amenable to quenching by the surface-charged CQDs. The data at 5 M urea validate this explanation, as evidenced by the steep decrease in CQDs-dose-dependent fluorescence intensity under unfolded (5 M urea) condition. The results of a study on the interactions between carbonaceous CQDs and human transferrin (hTf) or bovine serum albumin (BSA) proteins revealed that CQDs attach tightly to hTf and BSA (via hydrophobic forces) and cause structural alterations to both plasma proteins [37].

3.3. Impact of gelatin CQDs on the secondary structure

In order to evaluate the impact of CQDs on the secondary structure of a protein, we examined the CD spectra of apo-myoglobin as a function of CQDs dose (Fig. 7A) [75-78].

Visual inspection of CD spectra reveals distinct changes in secondary structure as a function of CQD dose. A diminution in the minima at 208 nm and 222 nm are visible as the CQDs dose increases from 0.1 mg. mL^{-1} to 1 mg. mL^{-1}. This feature is accompanied by an increase in the minima at 200 nm suggesting the gradual conversion of helical elements to disordered structures. The ablation at 208 nm and 222 nm is almost complete in the presence of 1 mg. mL^{-1} gelatin CQDs. Further quantitative analysis carried out using in silico online tool, BestSel, permitted quantification of alpha-helices, beta-sheets, turns, and unordered structures in apo-myoglobin +/− CQDs [78]. Fig. 7B is a graph of the deconvoluted equilibrium CD spectra as a function of gelatin CQDs concentration. A decline

in helix content (green) is observed with an increase in unordered structure. Factors that cause helix destabilization include pH, high temperature, and denaturing agents. Disruption in the helical structure of the apo-myoglobin can also occur due to unfavorable interactions between charged groups and the helix macrodipole. A research study aimed at investigating the interaction between carbonaceous dots and human transferrin (hTf) and albumin (BSA) revealed similar findings. When carbon dots were titrated into the protein solutions of BSA and hTf, a significant decrease in intensity was observed for the two negative peaks at 208 nm and 222 nm. This reduction in intensity indicates significant structural changes in both proteins, which led to the loss of α-helix contents within the proteins [37].

Both beta-sheet contents and turns are relatively unchanged and may fall within the measurement/fitting error.

An examination of the minima at 222 nm and 208 nm suggests a slight increase in the 222/208 ratio as a function of the CQDs (Table S1), suggesting a mechanism by which helices may eventually unwind to disordered structures. The 222/208 ratio indicates whether an isolated helix exists or several helices form a coiled-coil (bundle; Fig. S4 in ESM). In an isolated state, helices have a ratio of ~0.8, whereas coiled coils have a ratio >1 [79-81]. Therefore, the data are indicative of a mechanism in which gelatin-derived CQDs initiate a bundling of isolated helices into coiled coils prior to their dismantling to form unordered structures (Fig. 8). Coiled coils are maintained stable by a series of hydrophobic knobs-into-holes packing interactions along with inter-and intrastrand electrostatic interactions. Although the $\theta 222/\theta 208$ ratio in the native apo-Mb of the control group is also close to 1, the increase of coiled-coil conformation in apo-Mb treated with CQDs can be explained by many possible intramolecular complimentary charge-charge interaction between protein and CQDs. The presence of CQDs in the environment and their hydrophobic intramolecular interactions with native apo-Mb cab be a factor in favoring coiled-coil formation.

Table S1 summarizes these findings and includes RMSD and NRMSD values which indicate the goodness-of-fit between the experimental CD data (over the wavelength range of the measurement) and the theoretical CD spectra [73,75-78].

We also measured the impact of gelatin-derived CQDs on the CD spectra of partially-unfolded apo-myoglobin introduced into 1.5 M urea (Fig. 9A). The data revealed a diminution in helical content due to the presence of the denaturant (1.5 M urea, 0 mg. mL^{-1-} CQDs). The addition of CQDs resulted in further attrition of the helical fraction of apo-myoglobin, as previously observed in the absence of urea (Fig. 7B). However, in the presence of urea (1.5 M), the CQDs titration resulted in a concomitant increase in the beta-sheet content of apo-myoglobin at the expense of the helix (Fig. 9B). The disordered region remained somewhat unperturbed. These results indicate that in the presence of mildly denaturing conditions, the CQDs facilitated the conversion of helices to sheets. A study on the interaction between carbon dots and proteins reported a shift from helix contents to β structures in the secondary structure of the protein after the binding of carbon dots to the enzyme proteins [82].

The trend in the θ222/θ208 ratio upon titration of apo-myoglobin with CQDs differed from that observed in the absence of the denaturing agent (Fig. S5 in ESM). The ratio throughout the course of the CQDs titration remained below 1 (~0.8), suggesting the absence of coiled-coil structures as intermediates in the CQDs-driven transitioning of helices to sheets.

Table S2 summarizes these findings and includes RMSD and NRMSD values which indicate the goodness-of-fit between the experimental CD data (over the wavelength range of the measurement) and the theoretical CD spectra.

To obtain chemical insight into the nature of interactions between CQDs and protein, FTIR spectra were obtained. The IR spectra and deconvolution analysis of the amide I region in native apo-myoglobin and apo-myoglobin treated with 0.5 and 1 mg. mL^{-1} gelatin CQDs are shown in Fig. 10. No obvious changes in this region were observed at CQDs concentrations lower than 0.5 mg. mL^{-1}. The recorded data in apo-myoglobin, both in the absence and presence of 0.5 and 1 mg. mL^{-1} gelatin CQDs, was in agreement with CD measurements. The deconvolution analysis of the amide I region in the absence of gelatin CQDs revealed a Gaussian component (25 % of the total peak areas) centered at 1654 cm^{-1}, which is typical of an α-helical conformation [83]. Gelatin CQDs attenuated this component by 10 and 20 % at doses of 0.5 and 1 mg. mL^{-1}, respectively. The maximum peak areas in apo-myoglobin treated with 0.5 mg. mL^{-1} CQDs were centered at 1645 cm^{-1}, which is typically assigned to unordered confirmation. These results suggest that in the presence of gelatin CQDs, apo-myoglobin's native, alpha-helical structure undergoes conformational changes. Recently, an investigation into niobium pentoxide nanoparticles (Nb$_2$O$_5$ NPs) interaction with BSA and human serum albumin (HSA) demonstrated the structural perturbations of the protein molecules after interaction with NPs [71].

3.4. Impact of CQDs on myoglobin function

We determined the heme-binding kinetics of apo-myoglobin in +/− gelatin-derived CQDs [84-86]. Upon the introduction of heme to a solution of apo-myoglobin, two phases were observed: a fast phase (Fig. 11A) corresponding to heme binding to apo-myoglobin and a slower phase (Fig. 11B), which may reflect the reorganization of the formed myoglobin. A comparison of the fast phase data for the binding of heme in +/− CQDs revealed clear differences in the trajectory to saturation. The presence of the CQDs resulted in a slower binding of heme to apo-myoglobin. The rate constant for the binding of heme to apo-myoglobin in the presence of CQDs was determined to be 0.12 s^{-1} μM^{-1} which was lower than that for the binding of heme to apo-myoglobin alone (0.56 s^{-1} μM^{-1}). The slow reorganization of bound heme was also impacted by the presence of CQDs. An examination of the slopes of the slow phase revealed that the rearrangement of the heme group was modulated by the presence of the CQDs, resulting in a slower increase in absorbance (0.34 units/h) over the course of the rearrangement vs. 0.54 units/h in its absence. In another study monitoring the dynamics of heme binding to the human transferrin protein, UV–Vis spectra showed a decrease in the characteristic peak (λ_{max} = 475 nm) intensity due to the interaction with carbon dots. This reduction in peak intensity during carbon dot titration suggests a change in the iron chemical environment of hTf and indicates the release of Fe^{+3} from hTf [37].

The interaction of nanoparticles with heme-containing proteins exhibited similar disruptive effects of these materials on heme binding or activity [87]. A study on metal-based nanoparticles demonstrated their potential to hinder the activity of heme-dependent enzymes, such as CAT and cytochrome P450s [88], and interfere with heme production itself. Another study on the interaction between zero valent iron (ZVFe) nanoparticles and human hemoglobin (Hb) resulted in the displacement and breakdown of heme, thereby triggering protein carbonylation; an indicator of protein damage caused by reactive oxygen species (ROS) [89]. Morover, the interaction of nanoparticles with heme-containing proteins, such as cytochrome c, induced significant conformational changes in the structure of these proteins, affecting their active sites and overall structural stability [90].

3.5. Cytotoxicity of gelatin CQDs

Cytotoxicity of gelatin CQDs was evaluated using a neuroblastoma-derived cell line (SH-SY5Y) [20]. The results, shown in Fig. 12A, revealed no significant change in cell viability upon the addition of gelatin CQDs up to a concentration of 5 mg. mL^{-1} compared with the untreated and vehicle groups. Hydrogen peroxide (H$_2$O$_2$ 10 μM) was used as the positive control. These results revealed that gelatin CQDs are biocompatible up to a concentration of 5 mg. mL^{-1} (Fig. 12A).

Fig. 12 shows the images of the control, CQDs-treated (10 mg. mL^{-1}), and H$_2$O$_2$ groups in panels B, C, and D, respectively. Propidium iodide dyes (staining the nuclei of necrotic or dead cells due to lack of membrane integrity), and Hoechst dyes (staining the nuclei of normal cells, as Hoechst 33342 is significantly cell-permeable due to the addition of a lipophilic ethyl group and is usually preferred for living cell staining) at a final concentration of 1 μg. mL^{-1} each, were added to each well 1 h prior to obtaining readings. As shown in Fig. 12C, the CQDs-treated cells' viability is similar to the control group (Fig. 12B) and is another fact of secured cells upon the addition of CQDs. As previously demonstrated, carbon quantum dots cause minimal toxicity towards most cell lines, with only slight residual toxicity observed at higher nanoparticle concentrations [91,92].

3.6. Conclusion

Using a biologically essential protein as a model, this work examines the molecular impact of CQDs on its structure and function.

Gelatin-derived CQDs were synthesized and characterized to address their impact on apo-myoglobin structure and function. The tertiary structures of apo-myoglobin (and myoglobin) are key to heme-binding, which regulates myoglobin's role as an oxygen-storage protein. A CQDs dose-dependent red-shift in the intrinsic fluorescence emission of apo-myoglobin suggested that the nanomaterials cause the protein to unfold (Fig. S3). An increase in emission intensity was also concomitantly observed, suggesting that the Trp residue, whose fluorescence is quenched by histidine and amide moieties, was becoming uncoupled by the addition of CQDs [73,74]. The process continued until high denaturant concentrations resulted in the unfolding of apo-myoglobin and the direct quenching of fluorescence by the CQDs (Fig. 6).

Next, we addressed the role of CQDs on the secondary structure of apo-myoglobin. Apo-myoglobin was chosen to limit CQDs' impact on helices structure. An increase in the CQDs concentration led to shifts in ellipticity at 208 and 222 nm towards less negative values, indicative of decreasing the alpha-helical content of the protein. Therefore, the CQDs dose-dependent diminution in the helix content of apo-myoglobin is likely induced by the highly negatively charged CQDs surfaces interacting with the helices of apo-myoglobin [93-97]. Under native experimental conditions (absence of denaturing agent; Table S1), the θ222/θ208 ratio, reflecting the transition between the single helices and coiled-coil (superhelical confirmation), increased as a result of increasing the CQDs concentration [98] (Fig. 8). The interaction of functional groups on the surface of carbon quantum dots with the N or C domain of protein may also lead to changes in the domain arrangement of the protein and eventually affect its secondary structure [79,98-100]. By contrast, in semi-folded protein (in the presence of limited denaturant), this ratio was not affected significantly by CQDs treatment (Table S2) and was less than the native state, indicating that partial unfolding of apo-myoglobin leads to a reduction in its inter-helical interactions [98]. Importantly, in this scenario, the loss of helices leads to the formation of beta structures.

The IR data centered around the amide I region corroborated the CD findings. Importantly, an examination of the heme-binding ability of myoglobin, a key feature required for oxygen storage, was disrupted by the presence of gelatin-derived CQDs, suggesting that the CQDs disrupt myoglobin function. It is likely that structural compromise, as evidenced by fluorescence, CD, and IR readouts is the underlying cause for perturbed heme binding to apo-myoglobin.

Lastly, consistent with previous findings [1,16,19-22,29], the CQDs showed low cytotoxicity to the cells. Also, in agreement with other reports, the data revealed a concentration-dependent cytotoxic response of carbon quantum dots, demonstrating that the concentration of CQDs is one of the main factors affecting their cytotoxicity against cells.

In this study, by using tertiary and secondary structural outputs coupled with protein functional group signatures, we were able to advance a molecular understanding of the impact of CQDs on a model protein structure. Importantly, the structural perturbations induced by the gelatin-derived CQDs resulted in functional compromises and important findings.

Limitations of the study

1. While the study elucidated the molecular impact of CQDs on the protein structure and function, further studies need to be extended in other types of protein structures, including beta-sheets, molten-globule states, intrinsically disordered proteins, and intermediates that populate folding trajectories other biomolecules like DNA, carbohydrates, or lipids. Understanding the broader implications of CQDs on diverse cellular components would provide a more comprehensive insight into their atomic and molecular effects within biological systems.

2. Although the study successfully correlated structural alterations induced by CQDs with functional compromises in myoglobin, the exploration was confined to a specific protein's heme-binding ability. Investigating a wider range of functional aspects of various proteins affected by CQDs could provide deeper insights into their impact on cellular functions.

3. While the study emphasized the low cytotoxicity of CQDs, future studies should delve deeper into the environmental and health impacts of CQDs and similar carbon nanomaterials, evaluating their effects on diverse cellular components and ecological systems to better define their implications.

4. The impact of physicochemical parameters such as pH, different buffers, metal ions, etc., is indeed crucial within physiological systems and has specific effects on the interaction between CQDs and the protein structure. These effects could potentially play critical roles in modulating the behavior of biomolecules. These factors may influence the stability and conformational changes of proteins, thereby warranting careful examination in subsequent studies.

Overall, these findings demonstrate the importance for more extensive studies to understand how these nanomaterials interact at the molecular level, ensuring their safe and effective application across various domains.

Supplementary Material

Refer to Web version on PubMed Central for supplementary material.

Funding

Data availability

Data will be made available on request.

References

[1]. Molaei MJ, Carbon quantum dots and their biomedical and therapeutic applications: a review, RSC Adv. 9 (12) (2019) 6460–6481. [PubMed: 35518468]

[2]. Sachdev A, Gopinath P, Green synthesis of multifunctional carbon dots from coriander leaves and their potential application as antioxidants, sensors and bioimaging agents, Analyst 140 (12) (2015) 4260–4269. [PubMed: 25927267]

[3]. Dehghani A, Ardekani SM, Hassan M, Gomes VG, Collagen derived carbon quantum dots for cell imaging in 3D scaffolds via two-photon spectroscopy, Carbon 131 (2018) 238–245.

[4]. Castro E, Cerón MR, Garcia AH, Kim Q, Etcheverry-Berríos A, Morel MJ, Díaz-Torres R, Qian W, Martinez Z, Mendez L, A new family of fullerene derivatives: fullerene-curcumin conjugates for biological and photovoltaic applications, RSC Adv. 8 (73) (2018) 41692–41698. [PubMed: 31543960]

[5]. Yang S-T, Cao L, Luo PG, Lu F, Wang X, Wang H, Meziani MJ, Liu Y, Qi G, Sun Y-P, Carbon dots for optical imaging in vivo, J. Am. Chem. Soc 131 (32) (2009)11308–11309. [PubMed: 19722643]

[6]. Ludmerczki R, Mura S, Carbonaro CM, Mandity EM, Carraro M, Senes N, Garroni S, Granozzi G, Calvillo L, Marras S, Carbon dots from citric acid and its intermediates formed by thermal decomposition, Chemistry–A Eur. J 25 (51) (2019)11963–11974.

[7]. Xu Q, Cai W, Li W, Sreeprasad TS, He Z, Ong W-J, Li N, Two-dimensional quantum dots: fundamentals, photoluminescence mechanism and their energy and environmental applications, Mater. Today Energy 10 (2018) 222–240.

[8]. Devi S, Gupta RK, Paul A, Kumar V, Sachdev A, Gopinath P, Tyagi S, Ethylenediamine mediated luminescence enhancement of pollutant derivatized carbon quantum dots for intracellular trinitrotoluene detection: soot to shine, RSC Adv. 8 (57) (2018) 32684–32694. [PubMed: 35547677]

[9]. Li H, Zhang Y, Ding J, Wu T, Cai S, Zhang W, Cai R, Chen C, Yang R, Synthesis of carbon quantum dots for application of alleviating amyloid-β mediated neurotoxicity, Colloids Surf. B Biointerfaces 212 (2022) 112373. [PubMed: 35101826]

[10]. Wang L, Li X, Han Y, Wang T, Zhao Y, Ali A, El-Sayed NN, Shi J, Wang W, Fan C, Quantum dots protect against MPP+-induced neurotoxicity in a cell model of Parkinson's disease through autophagy induction, SCIENCE CHINA Chem. 59 (11) (2016) 1486–1491.

[11]. Lu Y, Wang J, Yuan H, Xiao D, Separation of carbon quantum dots on a C18 column by binary gradient elution via HPLC, Anal. Methods 6 (20) (2014) 8124–8128.

[12]. Liu J-H, Cao L, LeCroy GE, Wang P, Meziani MJ, Dong Y, Liu Y, Luo PG, Sun Y-P, Carbon "quantum" dots for fluorescence labeling of cells, ACS Appl. Mater. Interfaces 7 (34) (2015) 19439–19445. [PubMed: 26262834]

[13]. Ye Y, Landa EN, Cantu JM, Hernandez-Viezcas JA, Nair AN, Lee W-Y, Sreenivasan ST, Gardea-Torresdey JL, A double-edged effect of manganese doped graphene quantum dots on salt-stressed Capsicum annuum L, Sci. Total Environ 844 (2022) 157160. [PubMed: 35798116]

[14]. Wang H, Zhang M, Ma Y, Wang B, Huang H, Liu Y, Shao M, Kang Z, Carbon dots derived from citric acid and glutathione as a highly efficient intracellular reactive oxygen species scavenger for alleviating the lipopolysaccharide-induced inflammation in macrophages, ACS Appl. Mater. Interfaces 12 (37) (2020) 41088–41095. [PubMed: 32805964]

[15]. Ren J, Malfatti L, Innocenzi P, Citric acid derived carbon dots, the challenge of understanding the synthesis-structure relationship, C 7 (1) (2020) 2.

[16]. Guerrero ED, Lopez-Velazquez AM, Ahlawat J, Narayan M, Carbon quantum dots for treatment of amyloid disorders, ACS Appl. Nano Mater 4 (3) (2021) 2423–2433. [PubMed: 33969279]

[17]. Mukherjee A, Sarkar N, A facile one-pot synthesis of water-soluble CQDs for the evaluation of their anti-amyloidogenic propensity, Mater. Adv 4 (9) (2023) 2106–2118.

[18]. Luo H, Li B, Liu J, Liu Y, Xiao Q, Huang S, Investigation on conformational variation and fibrillation of human serum albumin affected by molybdenum disulfide quantum dots, Int. J. Biol. Macromol 190 (2021) 999–1006. [PubMed: 34487782]

[19]. Henriquez G, Ahlawat J, Fairman R, Narayan M, Citric acid-derived carbon quantum dots attenuate Paraquat-induced neuronal compromise in vitro and in vivo, ACS Chem. Nerosci 13 (16) (2022) 2399–2409.

[20]. Ahlawat J, Henriquez G, Varela-Ramirez A, Fairman R, Narayan M, Gelatin-derived carbon quantum dots mitigate herbicide-induced neurotoxic effects in vitro and in vivo, Biomater. Adv 137 (2022) 212837. [PubMed: 35929242]

[21]. Ahlawat J, Narayan M, Multifunctional carbon quantum dots prevent soluble-to-toxic transformation of amyloid and oxidative stress, ACS Sustain. Chem. Eng 10 (14) (2022) 4610–4622.

[22]. Kim D, Yoo JM, Hwang H, Lee J, Lee SH, Yun SP, Park MJ, Lee M, Choi S, Kwon SH, Graphene quantum dots prevent α-synucleinopathy in Parkinson's disease, Nat. Nanotechnol 13 (9) (2018) 812–818. [PubMed: 29988049]

[23]. Mahmoudi M, Akhavan O, Ghavami M, Rezaee F, Ghiasi SMA, Graphene oxide strongly inhibits amyloid beta fibrillation, Nanoscale 4 (23) (2012) 7322–7325. [PubMed: 23079862]

[24]. Zhang W, Sigdel G, Mintz KJ, Seven ES, Zhou Y, Wang C, Leblanc RM, Carbon dots: a future Blood–Brain Barrier penetrating nanomedicine and drug nanocarrier, Int. J. Nanomedicine 16 (2021) 5003. [PubMed: 34326638]

[25]. Du J, Xu N, Fan J, Sun W, Peng X, Carbon dots for in vivo bioimaging and theranostics, Small 15 (32) (2019) 1805087.

[26]. Liyanage PY, Zhou Y, Al-Youbi AO, Bashammakh AS, El-Shahawi MS, Vanni S, Graham RM, Leblanc RM, Pediatric glioblastoma target-specific efficient delivery of gemcitabine across the blood–brain barrier via carbon nitride dots, Nanoscale 12 (14) (2020) 7927–7938. [PubMed: 32232249]

[27]. Li S, Peng Z, Dallman J, Baker J, Othman AM, Blackwelder PL, Leblanc RM, Crossing the blood–brain–barrier with transferrin conjugated carbon dots: a zebrafish model study, Colloids Surf. B Biointerfaces 145 (2016) 251–256. [PubMed: 27187189]

[28]. Liu Y, Liu J, Zhang J, Li X, Lin F, Zhou N, Yang B, Lu L, Noninvasive brain tumor imaging using red emissive carbonized polymer dots across the blood–brain barrier, ACS Omega 3 (7) (2018) 7888–7896. [PubMed: 30087926]

[29]. Wang M, Sun Y, Cao X, Peng G, Javed I, Kakinen A, Davis TP, Lin S, Liu J, Ding F, Graphene quantum dots against human IAPP aggregation and toxicity in vivo, Nanoscale 10 (42) (2018) 19995–20006. [PubMed: 30350837]

[30]. Yao K, Lv X, Zheng G, Chen Z, Jiang Y, Zhu X, Wang Z, Cai Z, Effects of carbon quantum dots on aquatic environments: comparison of toxicity to organisms at different trophic levels, Environ. Sci. Technol 52 (24) (2018) 14445–14451. [PubMed: 30486644]

[31]. Wei P-F, Jin P-P, Barui AK, Hu Y, Zhang L, Zhang J-Q, Shi S-S, Zhang HR, Lin J, Zhou W, Differential ERK activation during autophagy induced by europium hydroxide nanorods and trehalose: maximum clearance of huntingtin aggregates through combined treatment, Biomaterials 73 (2015) 160–174. [PubMed: 26409001]

[32]. Song Y, Wang H, Zhang L, Lai B, Liu K, Tan M, Protein corona formation of human serum albumin with carbon quantum dots from roast salmon, Food Funct. 11 (3) (2020) 2358–2367. [PubMed: 32125329]

[33]. Chen D, Ganesh S, Wang W, Amiji M, Plasma protein adsorption and biological identity of systemically administered nanoparticles, Nanomedicine 12 (17) (2017) 2113–2135. [PubMed: 28805542]

[34]. Chen D, Ganesh S, Wang W, Amiji M, The role of surface chemistry in serum protein corona-mediated cellular delivery and gene silencing with lipid nanoparticles, Nanoscale 11 (18) (2019) 8760–8775. [PubMed: 30793730]

[35]. Xu Z-Q, Yang Q-Q, Lan J-Y, Zhang J-Q, Peng W, Jin J-C, Jiang F-L, Liu Y, Interactions between carbon nanodots with human serum albumin and γ-globulins: the effects on the transportation function, J. Hazard. Mater 301 (2016) 242–249. [PubMed: 26368798]

[36]. Zeinabad HA, Kachooei E, Saboury AA, Kostova I, Attar F, Vaezzadeh M, Falahati M, Thermodynamic and conformational changes of protein toward interaction with nanoparticles: a spectroscopic overview, RSC Adv. 6 (107) (2016) 105903–105919.

[37]. Garcia YS, Barros MR, Ventura GT, de Queiroz RM, Todeschini AR, Neves JL, Probing the interaction of carbonaceous dots with transferrin and albumin: impact on the protein structure and non-synergetic metal release, J. Mol. Liq 292 (2019) 111460.

[38]. Bhattacharya A, Chatterjee S, Khorwal V, Mukherjee TK, Luminescence turn-on/off sensing of biological iron by carbon dots in transferrin, Phys. Chem. Chem. Phys 18 (7) (2016) 5148–5158. [PubMed: 26606902]

[39]. Cao L, Li J, Song Y, Cong S, Wang H, Tan M, Molecular interaction of fluorescent carbon dots from mature vinegar with human hemoglobin: insights from spectroscopy, thermodynamics and AFM, Int. J. Biol. Macromol 167 (2021) 415–422. [PubMed: 33278433]

[40]. Song Y, Cao L, Li J, Cong S, Li D, Bao Z, Tan M, Interactions of carbon quantum dots from roasted fish with digestive protease and dopamine, Food Funct. 10 (6) (2019) 3706–3716. [PubMed: 31168551]

[41]. Gros G, Wittenberg BA, Jue T, Myoglobin's old and new clothes: from molecular structure to function in living cells, J. Exp. Biol 213 (16) (2010) 2713–2725. [PubMed: 20675540]

[42]. Kohn EM, Lee JY, Calabro A, Vaden TD, Caputo GA, Heme dissociation from myoglobin in the presence of the zwitterionic detergent N, N-dimethyl-N-Dodecylglycine betaine: effects of ionic liquids, Biomolecules 8 (4) (2018) 126. [PubMed: 30380655]

[43]. Barrick D, Baldwin RL, The molten globule intermediate of apomyoglobin and the process of protein folding, Protein Sci. 2 (6) (1993) 869–876. [PubMed: 8318892]

[44]. Majorina MA, Balobanov VA, Uversky VN, Melnik BS, Loops linking secondary structure elements affect the stability of the molten globule intermediate state of apomyoglobin, FEBS Lett. 594 (20) (2020) 3293–3304. [PubMed: 32770670]

[45]. Iannuzzi C, Maritato R, Irace G, Sirangelo I, Misfolding and amyloid aggregation of apomyoglobin, Int. J. Mol. Sci 14 (7) (2013) 14287–14300. [PubMed: 23839096]

[46]. Nagai M, Nagai Y, Imai K, Neya S, Circular dichroism of hemoglobin and myoglobin, Chirality 26 (9) (2014) 438–442. [PubMed: 24425582]

[47]. Kermani ZR, Haghighi SS, Hajihosseinali S, Fashami AZ, Akbaritouch T, Akhtari K, Shahpasand K, Falahati M, Aluminium oxide nanoparticles induce structural changes in tau and cytotoxicity of the neuroblastoma cell line, Int. J. Biol. Macromol 120 (2018) 1140–1148. [PubMed: 30179693]

[48]. Rahmani S, Mogharizadeh L, Attar F, Rezayat SM, Mousavi SE, Falahati M, Probing the interaction of silver nanoparticles with tau protein and neuroblastoma cell line as nervous system models, J. Biomol. Struct. Dyn 36 (15) (2018) 4057–4071. [PubMed: 29173031]

[49]. Wagner G, Perez M, Toscano W Jr., Gunsalus I, Apoprotein formation and heme reconstitution of cytochrome P-450cam, J. Biol. Chem 256 (12) (1981) 6262–6265. [PubMed: 6263910]

[50]. Chien S-C, Shoji O, Morimoto Y, Watanabe Y, Use of apomyoglobin to gently remove heme from a H 2 O 2-dependent cytochrome P450 and allow its reconstitution, New J. Chem 41 (1) (2017) 302–307.

[51]. Weitner T, Friganovi T, Šaki D, Inner filter effect correction for fluorescence measurements in microplates using variable vertical Axis focus, Anal. Chem 94 (19) (2022) 7107–7114. [PubMed: 35502461]

[52]. Hofbauer S, Howes BD, Flego N, Pirker KF, Schaffner I, Mlynek G, Djinovi -Carugo K, Furtmüller PG, Smulevich G, Obinger C, From chlorite dismutase towards HemQ–the role of the proximal H-bonding network in haeme binding, Biosci. Rep 36 (2) (2016).

[53]. Kawamura-Konishi Y, Kihara H, Suzuki H, Reconstitution of myoglobin from apoprotein and heme, monitored by stopped-flow absorption, fluorescence and circular dichroism, Eur. J. Biochem 170 (3) (1988) 589–595. [PubMed: 3338455]

[54]. Yu X-W, Liu X, Jiang Y-W, Li Y-H, Gao G, Zhu Y-X, Lin F, Wu F-G, Rose bengal-derived ultrabright sulfur-doped carbon dots for fast discrimination between live and dead cells, Anal. Chem 94 (10) (2022) 4243–4251. [PubMed: 35235297]

[55]. Prasad A, Sedlá ová M, Balukova A, Ovsii A, Rác M, K upka M, Kasai S, Pospíšil P, Reactive oxygen species imaging in U937 cells, Front. Physiol 11 (2020) 552569. [PubMed: 33178031]

[56]. De Hoon I, Barras A, Swebocki T, Vanmeerhaeghe B, Bogaert B, Muntean C, Abderrahmani A, Boukherroub R, De Smedt S, Sauvage F, Influence of the size and charge of carbon quantum dots on their corneal penetration and permeation enhancing properties, ACS Appl. Mater. Interfaces 15 (3) (2023) 3760–3771. [PubMed: 36645837]

[57]. Travlou NA, Giannakoudakis DA, Algarra M, Labella AM, Rodríguez-Castellón E, Bandosz TJ, S-and N-doped carbon quantum dots: surface chemistry dependent antibacterial activity, Carbon 135 (2018) 104–111.

[58]. Bing W, Sun H, Yan Z, Ren J, Qu X, Programmed bacteria death induced by carbon dots with different surface charge, Small 12 (34) (2016) 4713–4718. [PubMed: 27027246]

[59]. Yan J, Hou S, Yu Y, Qiao Y, Xiao T, Mei Y, Zhang Z, Wang B, Huang C-C, Lin C-H, The effect of surface charge on the cytotoxicity and uptake of carbon quantum dots in human umbilical cord derived mesenchymal stem cells, Colloids Surf. B Biointerfaces 171 (2018) 241–249. [PubMed: 30036791]

[60]. Kumar R, Kumar A, Verma N, Khopkar V, Philip R, Sahoo B, Ni nanoparticles coated with nitrogen-doped carbon for optical limiting applications, ACS Appl. Nano Mater 3 (9) (2020) 8618–8631.

[61]. Perikala M, Bhardwaj A, Highly stable white-light-emitting carbon dot synthesis using a non-coordinating solvent, ACS Omega 4 (25) (2019) 21223–21229. [PubMed: 31867516]

[62]. Zhang J-H, Niu A, Li J, Fu J-W, Xu Q, Pei D-S, In vivo characterization of hair and skin derived carbon quantum dots with high quantum yield as long-term bioprobes in zebrafish, Sci. Rep 6 (1) (2016) 1–12. [PubMed: 28442746]

[63]. Shabbir H, Csapo E, Wojnicki M, Carbon quantum dots: the role of surface functional groups and proposed mechanisms for metal ion sensing, Inorganics 11 (6) (2023) 262.

[64]. Yuan T, Meng T, He P, Shi Y, Li Y, Li X, Fan L, Yang S, Carbon quantum dots: an emerging material for optoelectronic applications, J. Mater. Chem C 7 (23) (2019) 6820–6835.

[65]. Ding H, Li X-H, Chen X-B, Wei J-S, Li X-B, Xiong H-M, Surface states of carbon dots and their influences on luminescence, J. Appl. Phys 127 (23) (2020).

[66]. Chu H-W, Unnikrishnan B, Anand A, Lin Y-W, Huang C-C, Carbon quantum dots for the detection of antibiotics and pesticides, J. Food Drug Anal 28 (4) (2020) 539. [PubMed: 35696146]

[67]. Yang X, Sun J, Cui F, Ji J, Wang L, Zhang Y, Sun X, An eco-friendly sensor based on CQD@MIPs for detection of N-acylated homoserine lactones and its 3D printing applications, Talanta 219 (2020) 121343. [PubMed: 32887072]

[68]. Zhu C, Zhai J, Dong S, Bifunctional fluorescent carbon nanodots: green synthesis via soy milk and application as metal-free electrocatalysts for oxygen reduction, Chem. Commun 48 (75) (2012) 9367–9369.

[69]. Li Y, Liu D, Wang Y-Q, Wang F-F, Qiu H-X, Eu 3+–functionalized CQD hybrid material: synthesis, luminescence properties and sensing application for the detection of Cu 2+, Mater. Adv 2 (10) (2021) 3346–3352.

[70]. Hsu P-C, Chang H-T, Synthesis of high-quality carbon nanodots from hydrophilic compounds: role of functional groups, Chem. Commun 48 (33) (2012) 3984–3986.

[71]. Millan S, Susrisweta B, Sahoo H, Probing the interaction between niobium pentoxide nanoparticles and serum albumin proteins by Spectroscopic approaches, J. Biomol. Struct. Dyn (2023) 1–11.

[72]. Randika Perera Y, Hill RA, Fitzkee NC, Protein interactions with nanoparticle surfaces: highlighting solution NMR techniques, Isr. J. Chem 59 (11–12) (2019) 962–979. [PubMed: 34045771]

[73]. Azami-Movahed M, Meratan AA, Ghasemi A, Ebrahim-Habibi A, Nemat-Gorgani M, Acetylation of lysine residues in apomyoglobin: structural changes, amyloid fibrillation, and role of surface charge, Int. J. Biol. Macromol 107 (2018) 626–634. [PubMed: 28919529]

[74]. Zhu Z, Wang Y, Kang Y, Zhang H, Zhang Z, Fei Z, Cao J, Graphene oxide destabilizes myoglobin and alters its conformation, Carbon 114 (2017) 449–456.

[75]. Laera S, Ceccone G, Rossi F, Gilliland D, Hussain R, Siligardi G, Calzolai L, Measuring protein structure and stability of protein–nanoparticle systems with synchrotron radiation circular dichroism, Nano Lett. 11 (10) (2011) 4480–4484. [PubMed: 21932791]

[76]. Greenfield NJ, Using circular dichroism spectra to estimate protein secondary structure, Nat. Protoc 1 (6) (2006) 2876–2890. [PubMed: 17406547]

[77]. Ianeselli A, Orioli S, Spagnolli G, Faccioli P, Cupellini L, Jurinovich S, Mennucci B, Atomic detail of protein folding revealed by an ab initio reappraisal of circular dichroism, J. Am. Chem. Soc 140 (10) (2018) 3674–3682. [PubMed: 29473417]

[78]. Micsonai A, Wien F, Kernya L, Lee Y-H, Goto Y, Réfrégiers M, Kardos J, Accurate secondary structure prediction and fold recognition for circular dichroism spectroscopy, Proc. Natl. Acad. Sci 112 (24) (2015) E3095–E3103. [PubMed: 26038575]

[79]. Gil-Garcia M, Navarro S, Ventura S, Coiled-coil inspired functional inclusion bodies, Microb. Cell Fact 19 (1) (2020) 1–16. [PubMed: 31898497]

[80]. Zhou NE, Zhu BY, Kay CM, Hodges RS, The two-stranded α-helical coiled-coil is an ideal model for studying protein stability and subunit interactions, Biopolymers, Original Res. Biomol 32 (4) (1992) 419–426.

[81]. Zhou NE, Kay CM, Hodges RS, Synthetic model proteins: the relative contribution of leucine residues at the nonequivalent positions of the 3–4 hydrophobic repeat to the stability of the two-stranded. alpha.-helical coiled-coil, Biochemistry 31 (25) (1992) 5739–5746. [PubMed: 1610823]

[82]. Das S, Kaushik R, Goswami P, Multifaceted interaction studies between carbon dots and proteins of clinical importance for optical sensing signals, ACS Appl. Bio Mater 5 (2) (2022) 889–896.

[83]. Vilasi S, Iannuzzi C, Portaccio M, Irace G, Sirangelo I, Effect of trehalose on W7FW14F apomyoglobin and insulin fibrillization: new insight into inhibition activity, Biochemistry 47 (6) (2008) 1789–1796. [PubMed: 18205397]

[84]. Hofbauer S, Hagmüller A, Schaffner I, Mlynek G, Krutzler M, Stadlmayr G, Pirker KF, Obinger C, Daims H, Djinovi -Carugo K, Structure and heme-binding properties of HemQ (chlorite dismutase-like protein) from Listeria monocytogenes, Arch. Biochem. Biophys 574 (2015) 36–48. [PubMed: 25602700]

[85]. Santucci R, Ascoli F, La Mar GN, Parish DW, Smith KM, Horse heart myoglobin reconstituted with a symmetrical heme A circular dichroism study, Biophys. Chem 37 (1–3) (1990) 251–255. [PubMed: 2285786]

[86]. Santucci R, Ascoli F, La Mar GN, Pandey RK, Smith KM, Reconstitution of horse heart myoglobin with hemins methylated at 6-or 7-positions: a circular dichroism study, Biochimica Biophys. Acta (BBA) Protein Struct. Mol. Enzymol 1164 (2) (1993) 133–137.

[87]. Mansouri A, Mousavi M, Attar F, Saboury AA, Falahati M, Interaction of manganese nanoparticle with cytochrome c: a multi-spectroscopic study, Int. J. Biol. Macromol 106 (2018) 78–86. [PubMed: 28818722]

[88]. Cameron SJ, Sheng J, Hosseinian F, Willmore WG, Nanoparticle effects on stress response pathways and nanoparticle–protein interactions, Int. J. Mol. Sci 23 (14) (2022) 7962. [PubMed: 35887304]

[89]. Mirzaei S, Hadadi Z, Attar F, Mousavi SE, Zargar SS, Tajik A, Saboury AA, Rezayat SM, Falahati M, ROS-mediated heme degradation and cytotoxicity induced by iron nanoparticles: hemoglobin and lymphocyte cells as targets, J. Biomol. Struct. Dyn 36 (16) (2018) 4235–4245. [PubMed: 29195491]

[90]. Tarpani L, Bellezza F, Sassi P, Gambucci M, Cipiciani A, Latterini L, New insights into the effects of surface functionalization on the peroxidase activity of cytochrome c adsorbed on silica nanoparticles, J. Phys. Chem. B 123 (11) (2019) 2567–2575. [PubMed: 30807173]

[91]. Sharma N, Das GS, Yun K, Green synthesis of multipurpose carbon quantum dots from red cabbage and estimation of their antioxidant potential and biolabeling activity, Appl. Microbiol. Biotechnol 104 (2020) 7187–7200. [PubMed: 32572575]

[92]. Bhamore JR, Jha S, Park TJ, Kailasa SK, Green synthesis of multi-color emissive carbon dots from Manilkara zapota fruits for bioimaging of bacterial and fungal cells, J. Photochem. Photobiol. B Biol 191 (2019) 150–155.

[93]. Moerz ST, Huber P, Protein adsorption into mesopores: a combination of electrostatic interaction, counterion release, and van der Waals forces, Langmuir 30 (10) (2014) 2729–2737. [PubMed: 24571263]

[94]. Wei Q, Becherer T, Angioletti-Uberti S, Dzubiella J, Wischke C, Neffe AT, Lendlein A, Ballauff M, Haag R, Protein interactions with polymer coatings and biomaterials, Angew. Chem. Int. Ed 53 (31) (2014) 8004–8031.

[95]. Zheng K, Kapp M, Boccaccini AR, Protein interactions with bioactive glass surfaces: a review, Applied, Mater. Today 15 (2019) 350–371.

[96]. Zhou Z, Hartmann M, Progress in enzyme immobilization in ordered mesoporous materials and related applications, Chem. Soc. Rev 42 (9) (2013) 3894–3912. [PubMed: 23570038]

[97]. Gruian C, Boehme S, Simon S, Steinhoff H-J, Klare J, Assembly and function of the tRNA-modifying GTPase MnmE adsorbed to surface functionalized bioactive glass, ACS Appl. Mater. Interfaces 6 (10) (2014) 7615–7625. [PubMed: 24785159]

[98]. Sala FA, Valadares NF, Macedo JN, Borges JC, Garratt RC, Heterotypic coiled-coil formation is essential for the correct assembly of the septin heterofilament, Biophys. J Ill (12) (2016) 2608–2619.

[99]. Brandenburg E, von Berlepsch H, Gerling UI, Böttcher C, Koksch B, Inhibition of amyloid aggregation by formation of helical assemblies, Chemistry–A Eur. J 17 (38) (2011) 10651–10661.

[100]. Wuo MG, Mahon AB, Arora PS, An effective strategy for stabilizing minimal coiled coil mimetics, J. Am. Chem. Soc 137 (36) (2015) 11618–11621. [PubMed: 26340721]
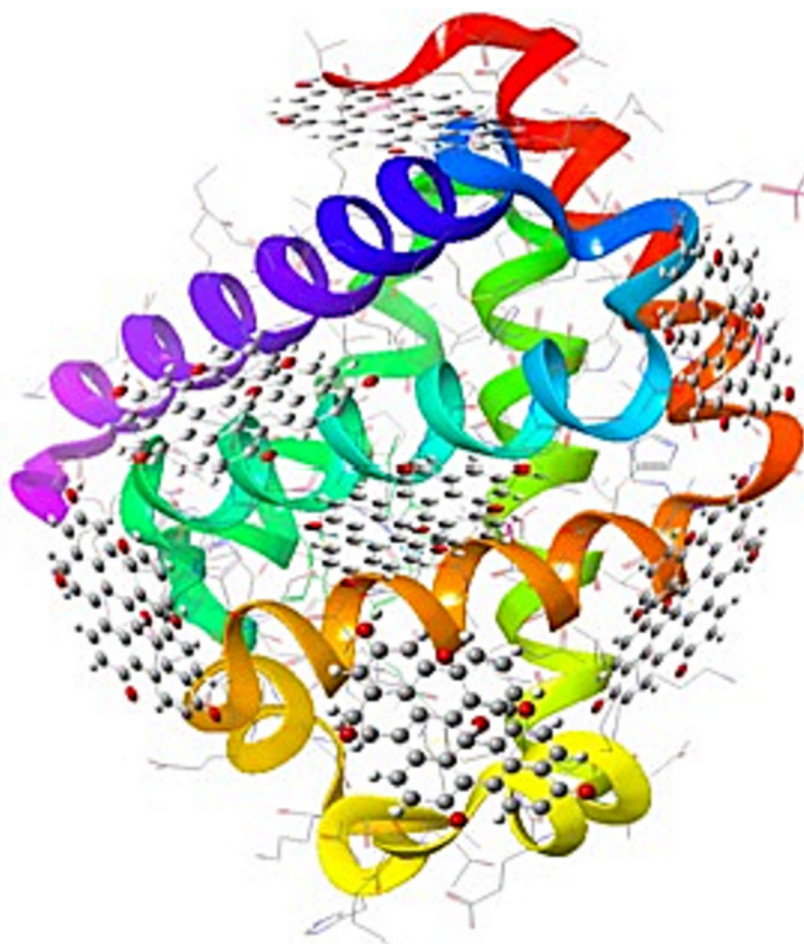
Fig. 1.
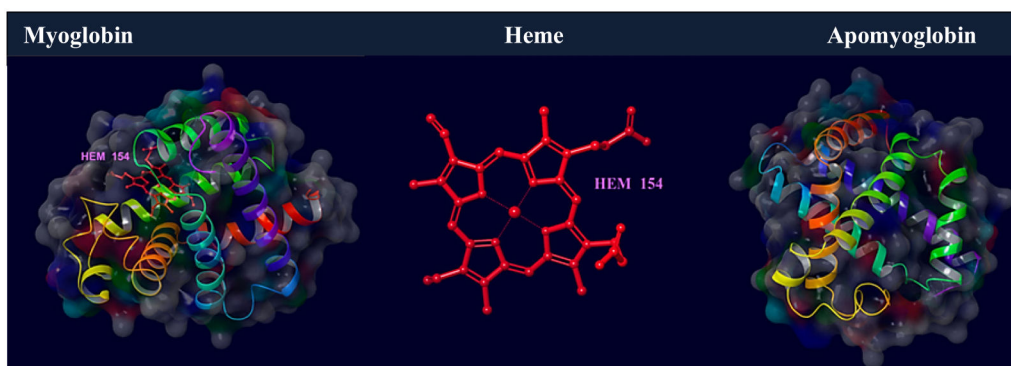The schematic of possible interactions between helices structures and CQDs.

Fig. 2.

Myoglobin, heme, and apo-myoglobin with the individual helices (Produced using the Maestro software).
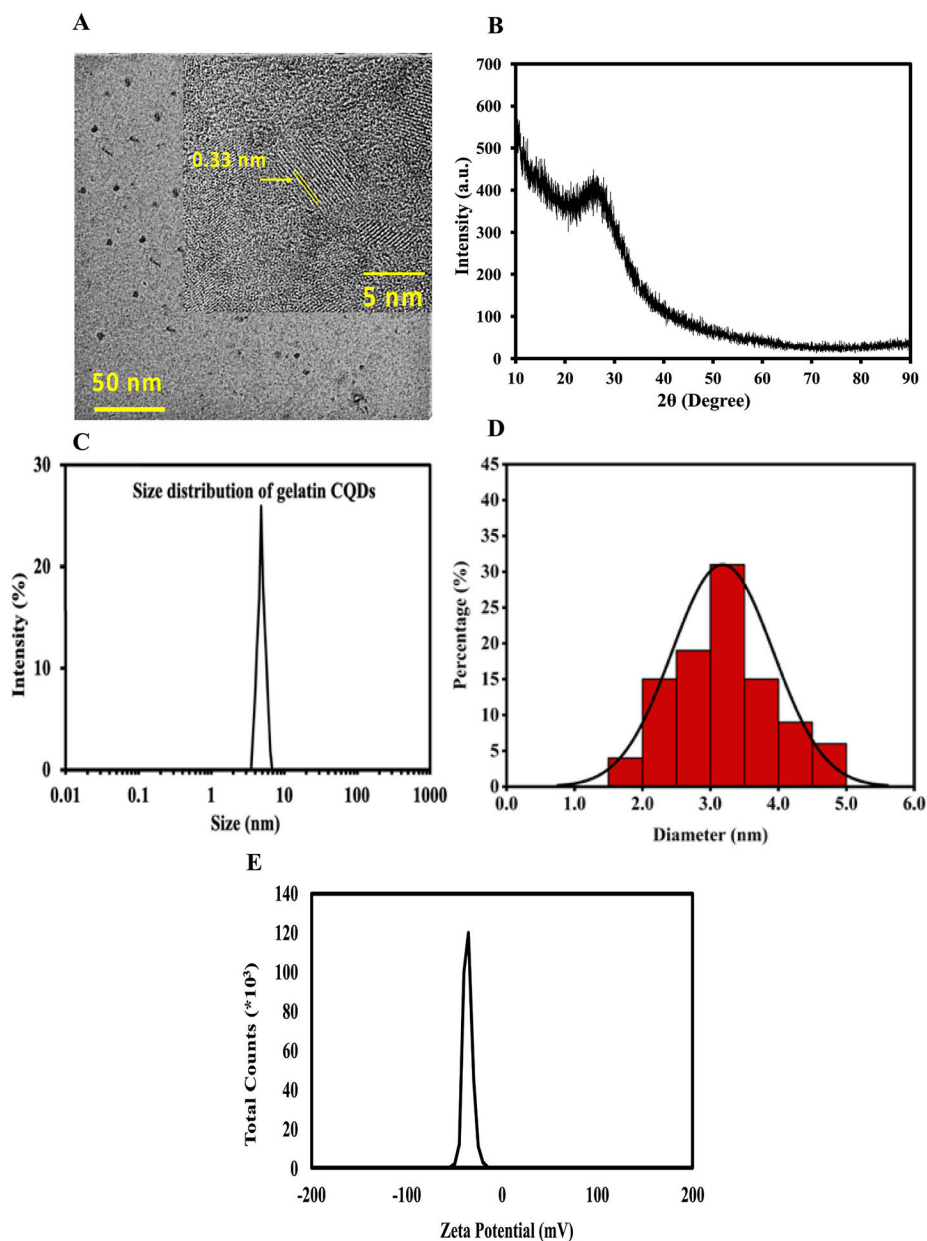
Fig. 3.
(A) HR-TEM images of gelatin CQDs, Inset shows lattice space image, (B) The XRD pattern of the as-synthesized CQDs, (C) DLS profile of gelatin CQDs, (D) Gaussian distribution of particles prepared using HR-TEM images with an average of around 3.5 nm. The distribution of particle sizes is observed around 4.8 nm., and (E) Zeta potential curve of the as-synthesized CQDs. The CQDs showed a negative surface charge of −35 mV.
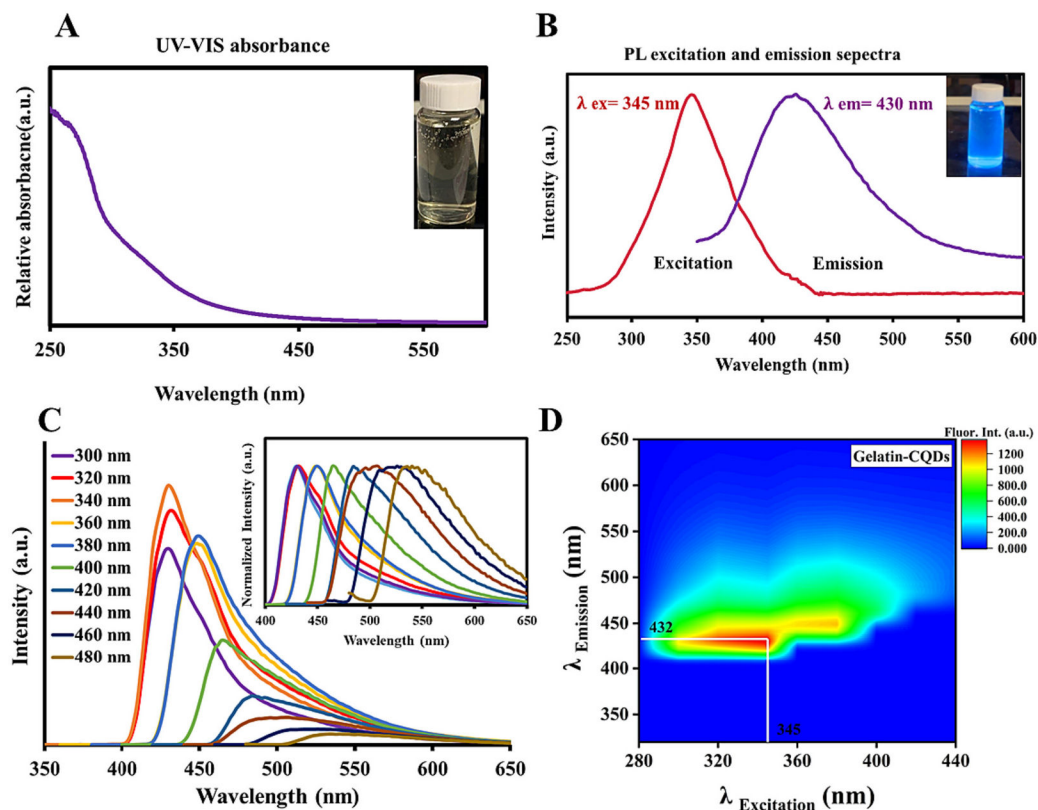
Fig. 4.
(A) UV–Vis absorption spectrum and the digital image of colorless CQDs solution as the inset, (B) The PL emission and excitation spectrum and UV-light image as the inset, (C) The PL spectra of the CQDs excited at different excitation wavelengths, and the inset shows the corresponding normalized PL emission, (D) The fluorescent contour map of gelatin CQDs.
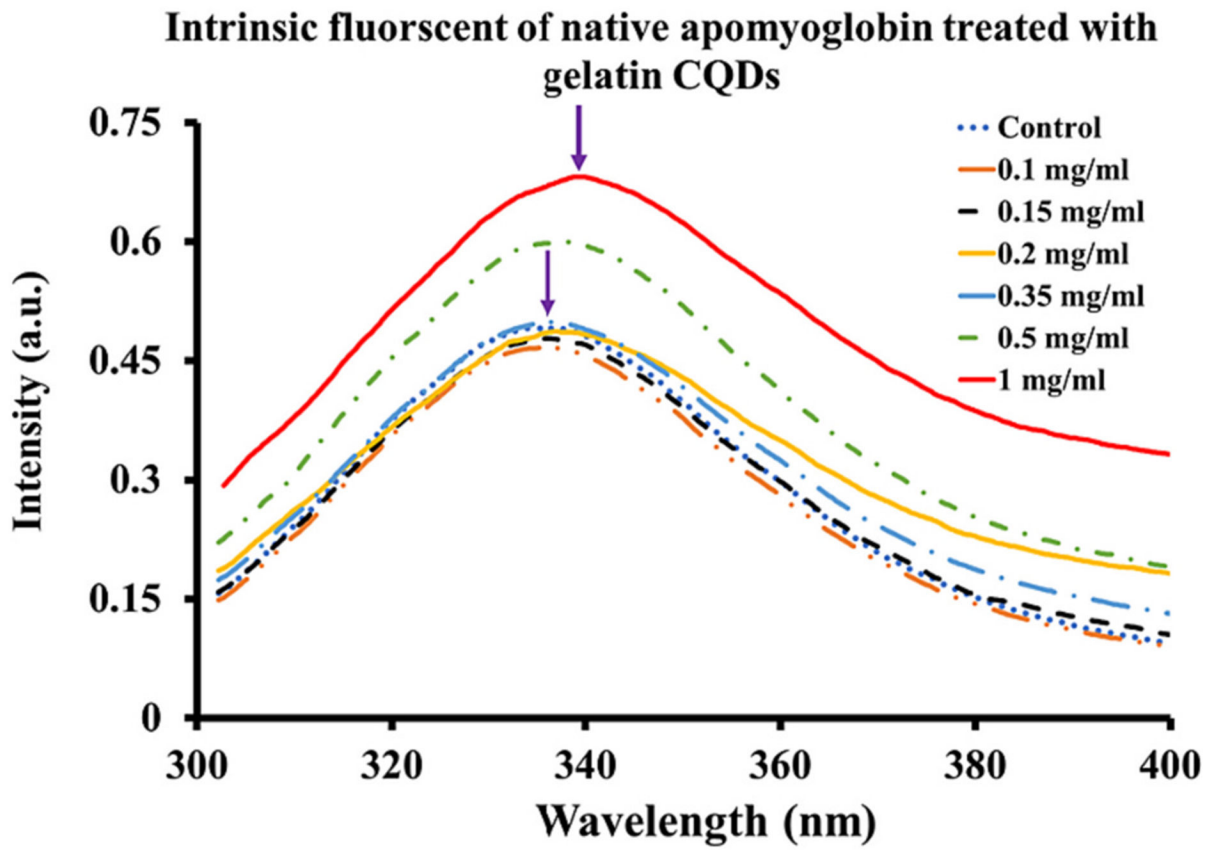
Fig. 5.
Steady-state fluorescence spectra for apo-myoglobin (λ ex = 280 nm) titrated with different concentrations of gelatin CQDs.
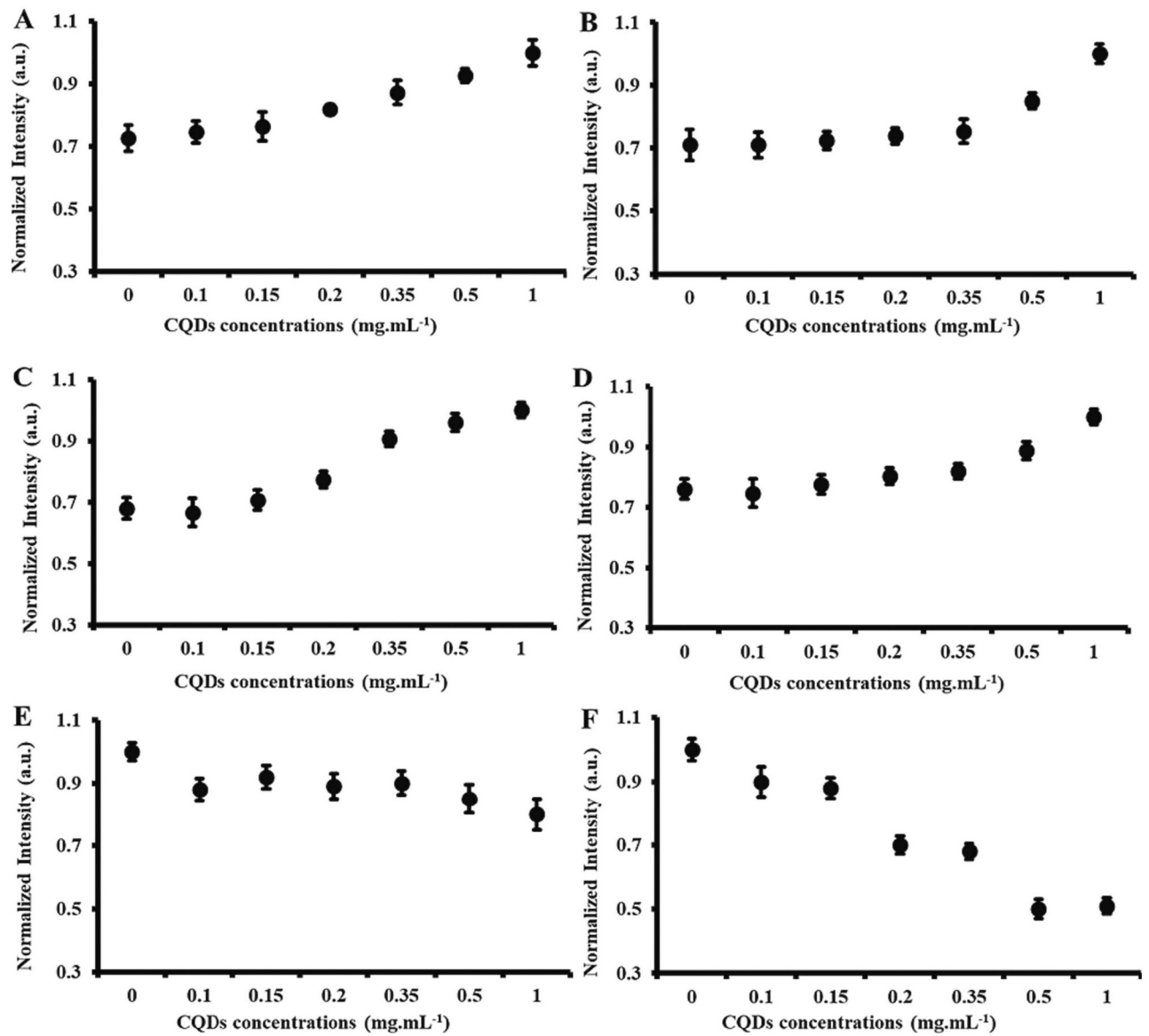
Fig. 6.
The normalized maximum intensity of urea-treated apo-myoglobin with gelatin CQDs (A) native state (B) 1 M urea (C) 2 M urea (D) 3 M urea (E) 4 M urea (F) 5 M urea.
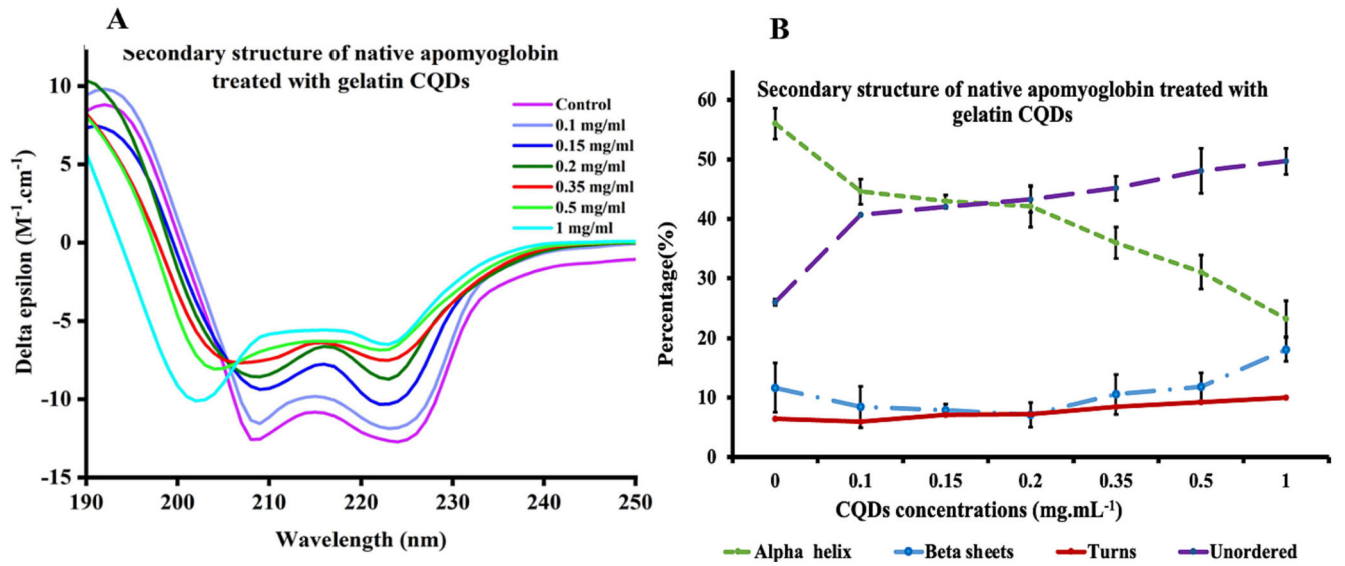
A

Secondary structure of native apomyoglobin treated with gelatin CQDs

Legend:
- Control
- 0.1 mg/ml
- 0.15 mg/ml
- 0.2 mg/ml
- 0.35 mg/ml
- 0.5 mg/ml
- 1 mg/ml

X-axis: Wavelength (nm)
Y-axis: Delta epsilon ($M^{-1}.cm^{-1}$)

B

Secondary structure of native apomyoglobin treated with gelatin CQDs

X-axis: CQDs concentrations ($mg.mL^{-1}$)
Y-axis: Percentage(%)

Legend:
- Alpha helix
- Beta sheets
- Turns
- Unordered

Fig. 7.

(A) CD Spectra of apo-myoglobin treated with different concentrations of gelatin CQDs

(B) The secondary structure and composition of native apo-myoglobin treated with different gelatin CQDs concentrations.

222:208 ratio>1
In presence of CQDs

Isolated Helix

Coiled coils Helices
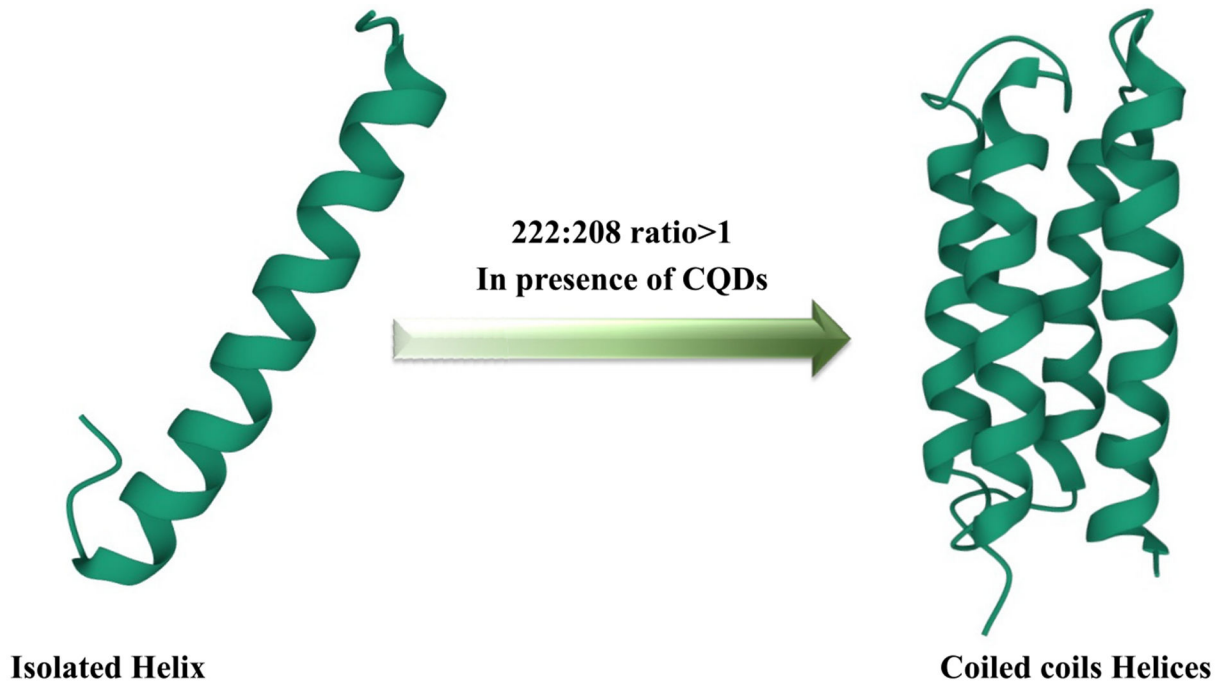
Fig. 8.
The transition between the isolated helix and coiled coils helices as a response to increasing concentrations of CQDs.
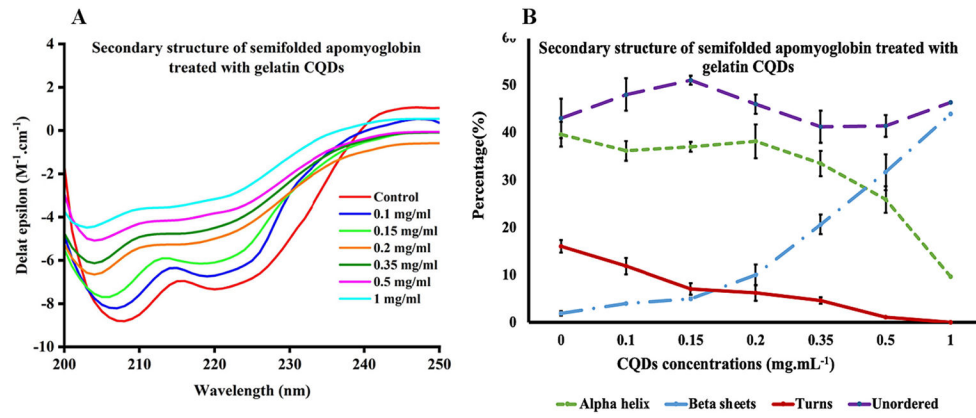
Fig. 9.

(A) CD Spectra of semi-folded apo-myoglobin treated with different concentrations of gelatin CQDs, (B) The secondary structure and composition of semi-folded apo-myoglobin treated with different gelatin CQDs concentrations.
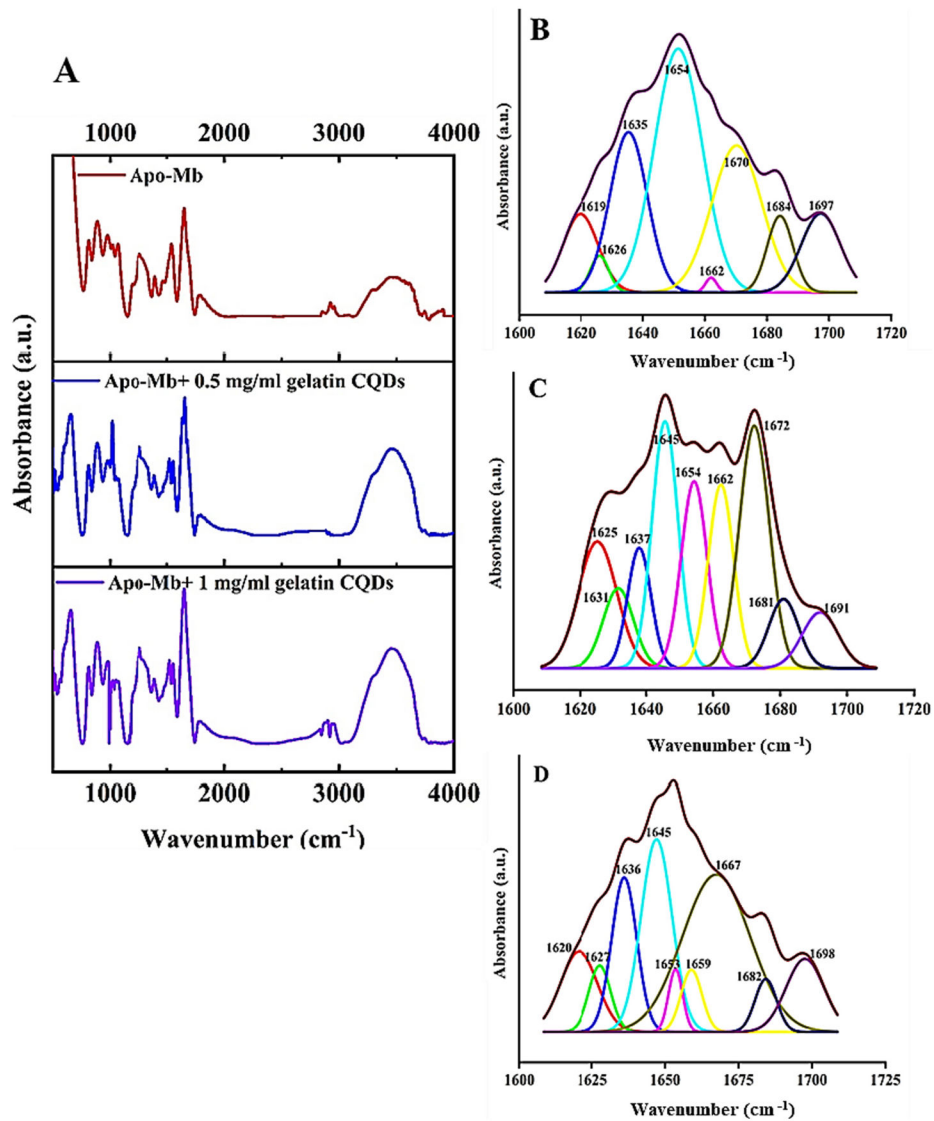
Fig. 10.
Deconvoluted IR spectrum of amid I region in (A) Whole IR spectra of (B) apo-myoglobin in the absence and (C) apo-myoglobin in the presence of 0.5 mg. mL^{-1} gelatin CQDs, and (D) apo-myoglobin in the presence of 1 mg. mL^{-1} gelatin CQDs.
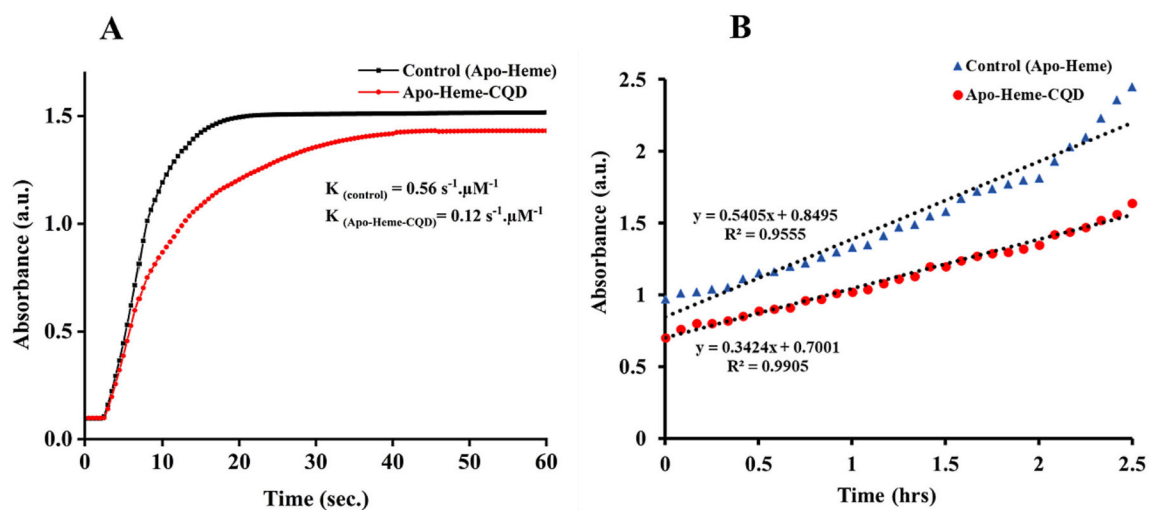
Fig. 11.
(A) The binding of heme to apo-myoglobin, evidenced by the increase in absorbance at 409 nm is seen in a fast phase. (B) The complex, now myoglobin, reorganizes over a much longer time scale.
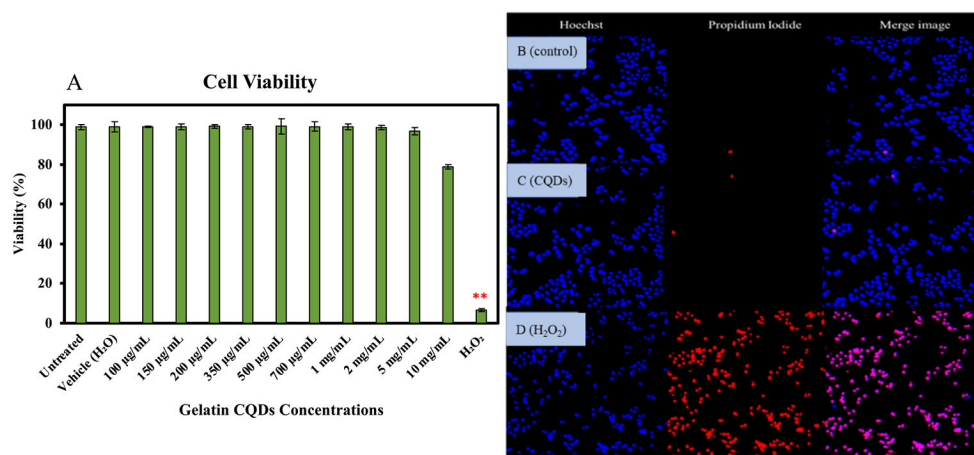
Fig. 12.
(A) Impact of gelatin CQDs (100 μg-10 mg. mL^{-1}) on the SHSY-5Y cell line viability. ** The mean difference is significant at the 0.01 level ($P < 0.01$). Hoechst-PI dual staining images of SHSY-5Y cells in B) untreated cells (negative control), C) cells treated with gelatin CQDs, and D) cells exposed to hydrogen peroxide (H_2O_2) (positive control).